

# The Hallmarks of Copper Single Atom Catalysts in Direct Alcohol Fuel Cells and Electrochemical CO<sub>2</sub> Fixation

*Izabela S. Pieta,\* Ravishankar G. Kadam, Piotr Pieta, Dusan Mrdenovic, Robert Nowakowski, Aristides Bakandritsos, Ondrej Tomanec, Martin Petr, Michal Otyepka, Robert Kostecki, M. A. Majeed Khan, Radek Zboril, and Manoj B. Gawande\**

Single-atom catalysts (SACs) are highly enviable to exploit the utmost utilization of metallic catalysts; their efficiency by utilizing nearly all atoms to often exhibit high catalytic performances. To architect the isolated single atom on an ideal solid support with strong coordination has remained a crucial trial. Herein, graphene functionalized with nitrile groups (cyanographene) as an ideal support to immobilize isolated copper atoms G(CN)-Cu with strong coordination is reported. The precisely designed mixed-valence single atom copper (G(CN)-Cu) catalysts deliver exceptional conversions for electrochemical methanol oxidation (MOR) and CO<sub>2</sub> reduction (CO<sub>2</sub>RR) targeting a “closed carbon cycle.” An onset of MOR and CO<sub>2</sub>RR are obtained to be ≈0.4 V and ≈−0.7 versus Ag/AgCl, respectively, with single active sites located in an unsaturated coordination environment, it being the most active Cu sites for both studied reactions. Moreover, G(CN)-Cu exhibited significantly lower resistivity and higher current density toward MOR and CO<sub>2</sub>RR than observed for reference catalysts.

“carbon-negative” manner.<sup>[1–6]</sup> Meanwhile, CO<sub>2</sub>RR can also reduce the global carbon footprint and remediate global climate change. Among SOM, bio-derived C<sub>1</sub>-C<sub>2</sub> alcohols (methanol, ethanol) and simple ethers (DME – dimethyl ether and DEE – diethyl ether) receive particular attention because they present several advantages comparing to hydrogen, that is, fuel storage safety.<sup>[7–11]</sup> Moreover, they can serve as drop-in-fuels, energy carriers, and hydrogen storage compounds suitable for internal or external reforming.<sup>[7–11]</sup>

The development of advanced fuel cells, based on bio-derived fuels and rationally designed catalytic nanostructured electrodes with a lowered amount of platinum group metals (PTG) and proven stability offers new opportunities for the applications of future sustainable energy.<sup>[1,2,12,13]</sup>


## 1. Introduction

The electrochemical CO<sub>2</sub> reduction reaction (CO<sub>2</sub>RR) to C<sub>1</sub>-C<sub>2</sub> hydrocarbon (HC) fuels and chemicals using surplus or renewable electricity, as well as the electrochemical conversion of small organic molecules (SOM) to sustainable energy, can be seen as a closed cycle strategy with maximized energy harvesting efficiency in a “carbon-neutral” or even a

For highly efficient energy conversion, it is crucial to progress the electrochemical devices, electrolytes, and electrochemical reaction procedures as well as tailor electrocatalysts' activity, considering both CO<sub>2</sub>RR and SOM electro-oxidation selectivities, and overcome kinetic limitations. Although extensively studied electro-oxidation reactions of methanol (MOR) was found to have more efficiency in alkaline than acidic media, the slow kinetic of MOR on the anode are among the

Dr. I. S. Pieta, Dr. P. Pieta, D. Mrdenovic, Prof. R. Nowakowski  
Institute of Physical Chemistry Polish Academy of Sciences  
Warsaw 01–224, Poland  
E-mail: ipieta@ichf.edu.pl

Dr. R. G. Kadam, Dr. A. Bakandritsos, O. Tomanec, M. Petr,  
Prof. M. Otyepka, Prof. R. Zbořil, Prof. M. B. Gawande  
Regional Centre of Advanced Technologies and Materials  
Palacky University  
Šlechtitelů 27, Olomouc 783 71, Czech Republic  
E-mail: manoj.gawande@upol.cz

 The ORCID identification number(s) for the author(s) of this article can be found under <https://doi.org/10.1002/admi.202001822>.

© 2021 The Authors. Advanced Materials Interfaces published by Wiley-VCH GmbH. This is an open access article under the terms of the Creative Commons Attribution-NonCommercial-NoDerivs License, which permits use and distribution in any medium, provided the original work is properly cited, the use is non-commercial and no modifications or adaptations are made.

The copyright line for this article was changed on 5 February 2021 after original online publication.

DOI: 10.1002/admi.202001822

Dr. P. Pieta, Dr. R. Kostecki  
Energy Storage & Distributed Resources Division  
Lawrence Berkeley National Laboratory  
1 Cyclotron Road, Berkeley, CA 94720, USA

Dr. A. Bakandritsos, Prof. R. Zbořil  
Nanotechnology Centre  
VŠB–Technical University of Ostrava  
17. listopadu 2172/15, Ostrava-Poruba 708 00, Czech Republic

Dr. M. A. Majeed Khan  
King Abdullah Institute for Nanotechnology  
King Saud University  
Riyadh, Saudi Arabia

Prof. M. B. Gawande  
Department of Industrial and Engineering Chemistry  
Institute of Chemical Technology Mumbai-Marathwada Campus  
Jalna, Maharashtra 431213, India

main problems in the application of direct alcohol fuel cells (DAFC).<sup>[1,2]</sup> Similarly, the critical CO<sub>2</sub>RR challenges concerns the electrocatalyst's and electrolyzer's designs, namely i) process selectivity enhancement, especially in a single-product Faradaic efficiency (FE) enhancement,<sup>[14]</sup> ii) energy efficiency improvement while reducing the over-potentials,<sup>[15,16]</sup> iii) system and operating cost reduction, by reaction protocols and rational catalysts design.<sup>[14–18]</sup>

A catalyst's activity, stability, resistance to poison, and selectivity play a crucial role in determining the rate of electrochemical reactions and overall process efficiency. Therefore, considerable research efforts have been devoted for the development of highly efficient and selective electrocatalysts as well as the design and fabrication of stable working electrodes.<sup>[2,15,19–21]</sup> Among the best-known catalysts, the PGM metals, such as Pt, Ru, Pd, and their alloys, exhibit relatively good activities. However, they are too exorbitant to be practically included in large-scale applications. Moreover, their simultaneous selective operation for different reactions is limited. Another problem is Pt catalysts poisoning. The MOR reaction intermediate, carbon monoxide (CO), binds strongly to the Pt catalyst and deactivates it. Notwithstanding, some newly established transition metals based catalysts, that is, Cu and Ni, exhibit encouraging properties, including satisfactory activity and durability.<sup>[1,2,15,22–24]</sup> However, the rational design of ideal electrode materials with low-cost, high activity, and good stability under applied conditions remains a formidable challenge.

Single atom catalysts (SACs) have attracted extensive attention considering every active atomic site is made accessible and provides the maximum atom utilization efficiency with high catalytic performance.<sup>[12,25–27]</sup> These properties make SACs highly distinctive from its bulk counterparts, and higher activities of such a material than those observed for pure metals are usually obtained for various reactions:<sup>[28]</sup> chemical (i.e., C–H activation,<sup>[29]</sup> selective oxidation aromatic alkanes at room temperature,<sup>[30]</sup> hydroxylation benzene to phenol,<sup>[31]</sup> the hydrogenative coupling of nitroarenes,<sup>[32]</sup> and alkene hydrosilylation<sup>[33]</sup>), electrochemical (i.e., CO<sub>2</sub>RR, oxygen reduction reaction (ORR), and nitrogen reduction reaction (NRR)), and photochemical (i.e., CO<sub>2</sub> conversion into chemical fuels).<sup>[34–37]</sup> However, synthesis of SACs to achieve all distinctive features together, including the selection of an appropriate solid support which can provide selective binding sites for a metal, strong interaction with support as the high surface energy of isolated atoms is always accountable for metal aggregation, and simple synthetic protocol remain great challenges.<sup>[38–40]</sup> Lately, numerous SACs have been fabricated by a conventional method which involves a high-temperature treatment which alters the properties of atomic sites and limits the catalytic activity. Currently, SACs have been widely utilized in electrocatalysis applications because of their extraordinary catalytic activity stability and selectivity.<sup>[41–43]</sup> In this regards, graphene-based 2D materials supported SACs have fascinated substantial research attention.<sup>[40,44–47]</sup> In an electrochemical application, SACs solve the problem of the PTG metal economy, decreasing amounts of the noble metal as an electrocatalyst, maintaining at the same time high activity. On the other hand, it has the potential to improve the electrocatalytic activity of cheaper, transition metal-based catalysts.<sup>[14,15,18,19,28,48]</sup>

For the CO<sub>2</sub>RR, the Ni-SACs are the most investigated formulation.<sup>[16]</sup> Apart from the Ni-SAC, Fe-based, and Co-based SACs also exhibit stable catalytic activities toward CO<sub>2</sub> to CO reduction.<sup>[49,50]</sup> However, to the best of our knowledge, there are rare research works that focus on the catalytic performance of transition metal-based SACs toward the SOM electro-oxidation. Remarkably, there is no systematic investigation of the reaction mechanism, rates, and kinetic limitations of transition metal based-SACs for the DAFCs application.

In the present work, a precisely designed mixed-valence single atom copper catalyst (G(CN)-Cu) delivering exceptional conversions for MOR and CO<sub>2</sub>RR is presented. The catalyst was prepared using our previously developed graphene derivative (cyanographene, G-CN),<sup>[12,48]</sup> exploiting the abundant cyano functionalities as selective and robust anchoring sites for atomically dispersed Cu. The G(CN)-Cu SAC contains ≈3.4 wt% Cu. Its performance has been compared with Cu/g-C<sub>3</sub>N<sub>4</sub> (Cu@g-C<sub>3</sub>N<sub>4</sub>, ≈4 wt% Cu)<sup>[1,2]</sup> reported previously, where rich electron lone pairs were determined to provide abundant uniform nitrogen coordinators for Cu isolated atoms. Herein, it is expected that both G-CN and g-C<sub>3</sub>N<sub>4</sub> could be a suitable electrocatalyst substrate for the MOR and CO<sub>2</sub>RR. Our results indicate that Cu metal atoms could strongly couple with the N atoms of G-CN and g-C<sub>3</sub>N<sub>4</sub>, exhibiting excellent electrical conductivity and superior catalytic activity in MOR and CO<sub>2</sub>RR. Remarkably, single Cu-atom-decorated G-CN (G(CN)-Cu) harbors the lowest limiting potential for both studied reactions.

## 2. Results and Discussion

### 2.1. Nanostructured Composites Characterization

The X-ray diffraction (XRD) pattern confirmed the absence of inorganic phases (**Figure 1a**).

The (001) reflection peak typical of fluorographene (FG) at  $2\theta = 14^\circ$ , has been vanished in intensity after the nucleophilic substitution. The (002) reflection peak of FG at  $2\theta = 25.7^\circ$  has shifted to a higher value of  $2\theta = 29.7^\circ$  for G-CN and G(CN)-Cu catalysts (**Figure S1**, Supporting Information), indicating a decrease in the d-spacing in the 2D structure stacking direction after the substitution reaction. The broadening of this peak also indicates the exfoliation of the G-CN sheets.<sup>[1]</sup> Transmission electron microscopy (TEM) also did not show any nanoparticles (**Figure 1b**). High-angle annular dark-field scanning transmission electron microscopy (HAADF-STEM) (**Figure 1c**) revealed that individual Cu atoms are uniformly dispersed on the G-CN sheets, and the bright spot highlighted by yellow circles in magnified HAADF-STEM images (**Figure 1d**) are Cu atoms. Though precise identification of the lighter elements is always a challenging task,<sup>[51]</sup> the elemental maps clearly confirmed the atomic and homogeneous dispersion of Cu SACs along with the presence of O, N, and C (**Figure 1e–i**). The single atomic nature of Cu SACs was confirmed by XANES/EXAFS techniques in our previous work.<sup>[12]</sup>

X-ray photoelectron spectroscopy (XPS) was implemented to investigate the chemical composition of G(CN)-Cu. The survey spectra (**Figure 2a**) and high-resolution X-ray photoelectron spectroscopy (HR-XPS) revealed the presence of mixed-valence state<sup>[52]</sup> of copper in which reduction of 30% Cu (II) ions to

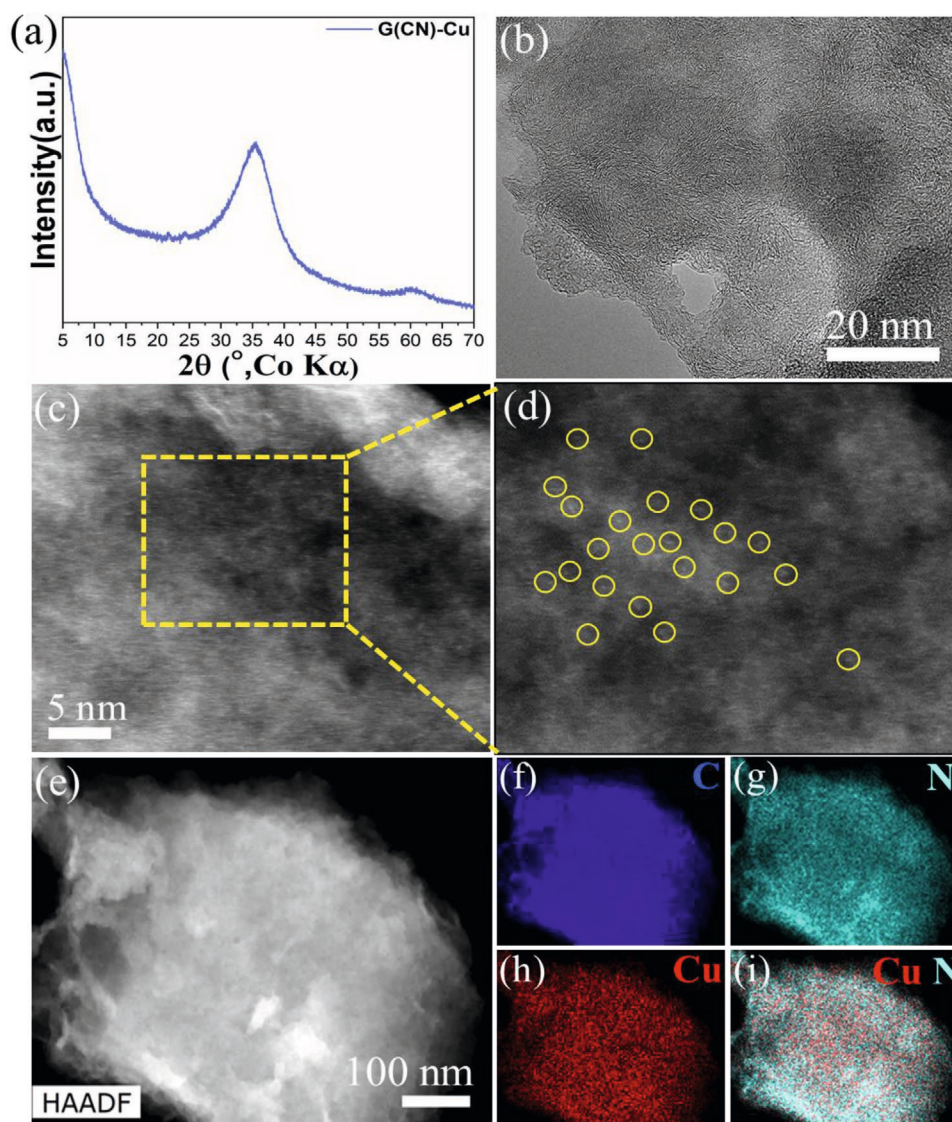


**Figure 1.** Characterization G(CN)-Cu SACs a) X-ray powder diffraction (XRD) pattern, b) TEM image, c) representative high-angle annular dark-field scanning transmission electron microscopy (HAADF-STEM) image, d) magnified HAADF-STEM image showing presence of single atom Cu (highlighted by a yellow circle). e) Another HAADF image of G(CN)-Cu and the corresponding EDS chemical mapping of G(CN)-Cu for C (blue) (f), N (cyan) (g), Cu (red) (h), and Cu (red) and N (cyan) together (i).

Cu(I) observed. The Cu 2p envelope (Figure 2b) indicated two valence states: Cu(I) at 932.6 eV and Cu (II) at 934.8 eV, with areas of 70% and 30%, individually, and the inset displays the corresponding deconvoluted spectrum for Cu<sub>2p<sub>3/2</sub></sub> peak (Figure 2b). Existence of the oxygen in G(CN)-Cu SACs survey spectra is probably due to the Cu single atoms having to complete the coordination sphere. Therefore, it is possible that Cu atoms can be coordinated with H<sub>2</sub>O and O<sub>2</sub> molecules, which is also explained in our previous work.<sup>[12]</sup>

The deconvolution of C 1s spectra (Figure S2a, Supporting Information) displayed distinct peaks with binding energies (BEs) of 284.82 and 286.01 that can be assigned for sp<sup>2</sup> C and sp<sup>3</sup> C atoms bond to -CN groups. The N1s spectrum (Figure S2b, Supporting Information) exhibits three peaks at 398.89, 400.52, and 401.31 eV corresponding to each of the different nitrogen functional groups, respectively.<sup>[12,18]</sup>

## 2.2. Morphology of Nanostructured Electrodes Characterization

AFM representative images of thin layers of G(CN)-Cu single-atom catalyst are shown in Figure 3 and Figures S3,S4, Supporting Information. The surface topology images (Figure 3a,b) clearly indicate the heterogeneity of the material, which contains two topologically different elements. The surface is dominated by amorphous areas (see, for example, the middle and bottom parts of the image Figure 3a). These places are characterized by a grain structure and, consequently, a considerable roughness (grain size in the range of several dozen nanometers). The second element of the layer has much smoother surfaces. These elements occur locally and geometrically correspond to aggregates of stacked nanoplates of the size of several hundred nanometers (see the upper part of images Figure 3a,b). The observed heterogeneity of the film is also confirmed by local

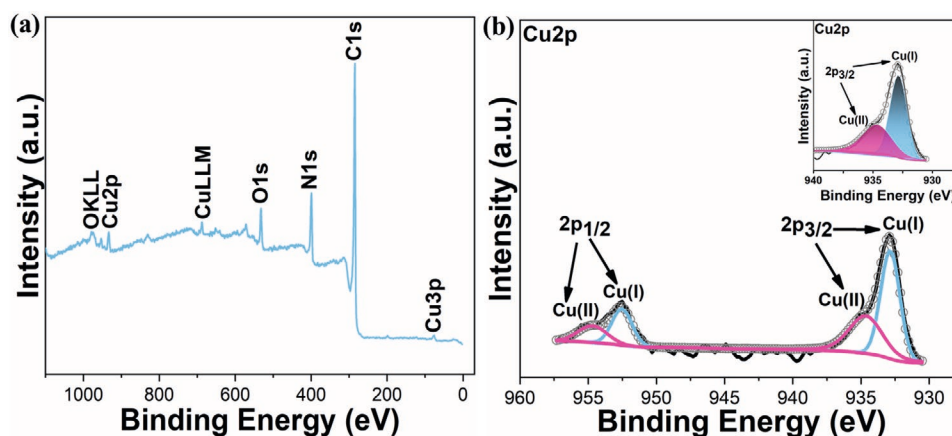


**Figure 2.** a) XPS survey spectra of G(CN)-Cu, and b) high-resolution Cu 2p, inset shows the separate corresponding spectrum for Cu2p<sub>3/2</sub> peak.

measurements of the surface mechanical properties. In this case, one can distinguish areas with significantly different rheological properties (Figure 3d). The surface is dominated by bright areas corresponding to a higher value of Young's modulus. However, locally, the places with a much lower value of the modulus are clearly distinguished (dark areas in the image).

It is worth noting that these differences are not directly correlated with the surface tilt. Generally, local changes of the surface slope, which is expected in such rough samples, can influence the effective area of the surface interaction with a microscope probe, which in turn may lead to changes in the locally registered values of rheological parameters. The surface profile (Figure 3c) corresponding to the white line in the image (Figure 3a) contains two segments marked with arrows (red and blue, respectively).

Both areas related to these sections are characterized in Figure 3d by similar but much lower with respect to the surrounding places' value of Young's modulus despite the fact that the surface tilt is significantly different. This is also visible in high resolution AFM images, Figures S3 and S4, Supporting Information. The above observation proves that the observed differences in the local rheological response correspond to real inhomogeneity of the surface of the tested catalyst layers.

### 2.3. Electrocatalytic Tests

The electrocatalytic performance of the G(CN)-Cu catalyst was evaluated by studying MOR and CO<sub>2</sub>RR and compared with

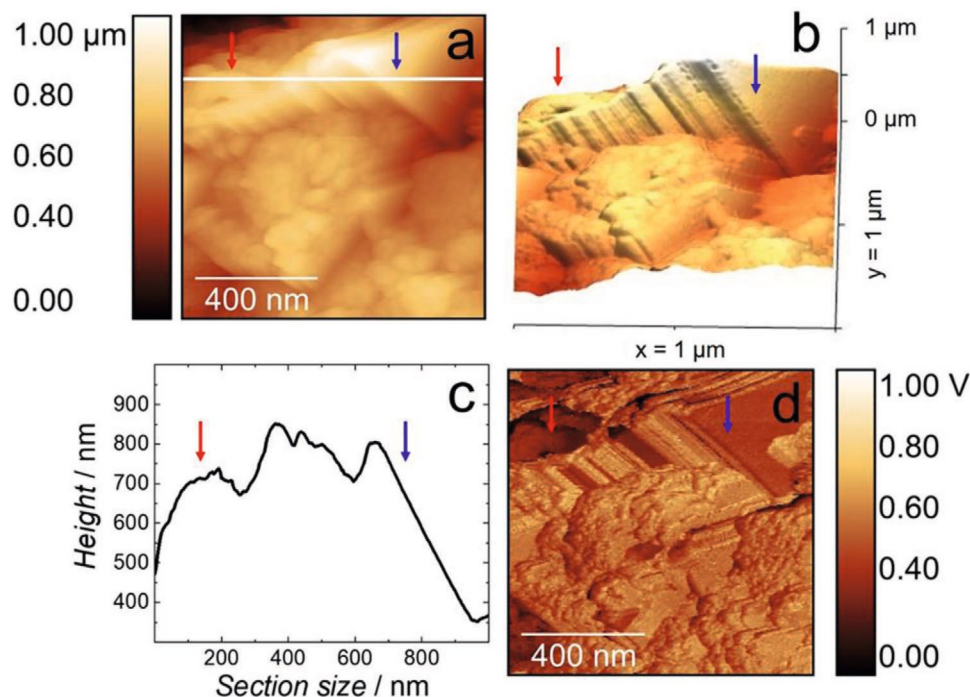


**Figure 3.** a) Topology and b) 3D model of a thin film of G(CN)-Cu single-atom catalyst. c) The cross-sectional profile of the topography map measured across the line shown in (a). d) Young's modulus map of G(CN)-Cu single-atom catalyst. The red and blue arrows point toward the amorphous and crystal phase.

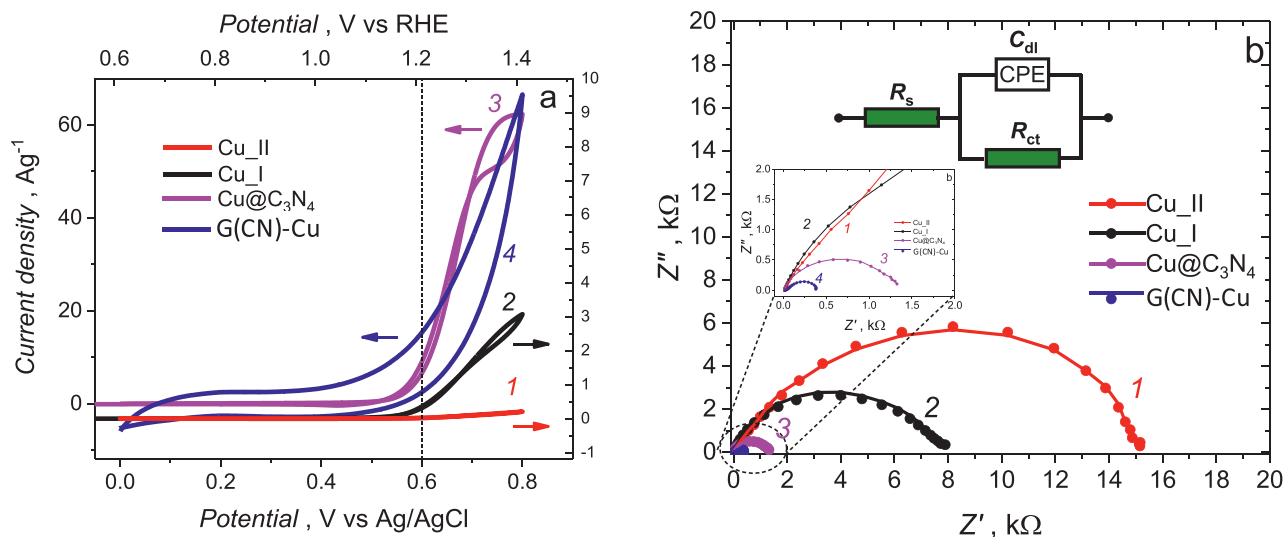


**Figure 4.** a) CV curves and b) Nyquist plot of Cu II (curve 1), Cu I (curve 2), Cu@C<sub>3</sub>N<sub>4</sub> (curve 3), and G(CN)-Cu (curve 4) in 1 M NaOH at 50 mV s<sup>-1</sup> scan rate. EIS spectra were recorded at E = 0.60 V versus Ag/AgCl. Experimental data points are indicated with filled circles, while solid curves are the numerical fitting to these points.

the reference Cu I, Cu II, and Cu@C<sub>3</sub>N<sub>4</sub> catalysts. Curves 4 in **Figure 4a,b** show electrochemical measurements for the GC electrode modified with the G(CN)-Cu catalyst film in terms of MOR.

CV measurements show that methanol undergoes catalytic electro-oxidation over the G(CN)-Cu catalyst in the potential range of 0 to 0.8 V versus Ag/AgCl. Notably, the onset of the catalytic oxidation is observed at ≈0.4 V versus Ag/AgCl. This potential onset is lower than that observed for Cu II, Cu I, and Cu@C<sub>3</sub>N<sub>4</sub> (curves 1, 2, and 3, respectively, in **Figure 4a**) as well as for Ni/gCN(H) previously reported.<sup>[1,2]</sup> The amplitude of the current density measured for G(CN)-Cu (curve 4 in **Figure 4a**) is comparable to that measured for Cu@C<sub>3</sub>N<sub>4</sub> (curve 3 in **Figure 4a**) but much higher than that measured for Cu II and Cu I (curve 1 and 2 in **Figure 4a**, respectively). Notably, the amount of Cu in the Cu@C<sub>3</sub>N<sub>4</sub> and G(CN)-Cu SACs is significantly lower than that of Cu I and Cu II, which indicates the excellent catalytic properties of both catalysts. This is confirmed by the lowest impedance for MOR determined at E = 0.60 V versus Ag/AgCl for G(CN)-Cu (curve 4 in **Figure 4b**), corresponding well with the CV results. An equivalent circuit model, shown as an inset in **Figure 4b**, was fit to each EIS spectrum. In this model,  $R_s$ ,  $CPE_{dl}$ , and  $R_{ct}$  represent an electrolyte resistivity, a constant phase element of experimental double-layer capacitance,  $C_{dl}$ , and an ohmic resistance of the charge transfer

of MOR, respectively. The values of  $R_{ct}$  obtained from the fitting are  $15.7 \pm 0.2$ ,  $7.7 \pm 0.3$ ,  $1.3 \pm 0.1$ , and  $0.37 \pm 0.01$  kΩ for Cu I, Cu II, Cu@C<sub>3</sub>N<sub>4</sub>, and G(CN)-Cu, respectively. As expected, the  $R_{ct}$  of the electrodes modified with Cu I, Cu II, and Cu@C<sub>3</sub>N<sub>4</sub> is significantly larger than that measured for G(CN)-Cu. Numerical results of the equivalent electric circuits fittings to the EIS data are given in **Table 1**.

**Figure 5a** shows LSV curves for the G(CN)-Cu catalyst in the absence (curve 1) and the presence of CO<sub>2</sub> (curve 2) as well as a reference to the G-CN support (curve 3). An apparent increase in the cathode current for a solution saturated with CO<sub>2</sub> (curve 2 in **Figure 5a**) compared to a solution saturated with Ar (curve 2 in **Figure 5a**) suggests the activity of the catalyst toward CO<sub>2</sub>RR.<sup>[6,15,18,49]</sup> The onset of CO<sub>2</sub>RR is observed at ≈-0.7 versus Ag/AgCl, which is comparable with the latest literature reports on Cu SAC.<sup>[6]</sup> **Figure 5b** shows LSV curves for the Cu I, Cu II, Cu@C<sub>3</sub>N<sub>4</sub>, and G(CN)-Cu catalysts (curve 1, 2, 3, and 4, respectively). Both Cu@C<sub>3</sub>N<sub>4</sub> and G(CN)-Cu catalysts show much better performance toward CO<sub>2</sub>RR in terms of the CO<sub>2</sub>RR potential onset and the amplitude of the currents than the reference Cu I and Cu II catalysts as well as SACs previously reported (**Table 2**).<sup>[6]</sup>

For G(CN)-Cu, similarly, as for the Ni-, Fe- or Co-SACs the activity can be linked to the active site structure, where the cooperation of Cu(II) – Cu(I) – support is the essential in the reaction

**Table 1.** Numerical results of the equivalent electric circuits fitting to the EIS data ( $R_s$ -an electrolyte resistivity, CPE-a constant phase element of experimental double-layer capacitance,  $C_{dl}$ ,  $R_{ct}$ -an ohmic resistance of the charge transfer of MOR, and  $\alpha$  is the frequency dispersion constant. (If  $\alpha$  is close to 1, CPE is dominated by capacitance. If  $\alpha$  is close to 0, CPE is dominated by resistance).

	$R_s$ [Ω]	CPE	$\alpha$	$R_{ct}$ [Ω]
Cu I	15.8 ± 0.9	5.8E-6 ± 0.2E-6	0.94 ± 0.01	15.7 ± 0.2
Cu II	15.3 ± 0.2	6.6E-6 ± 0.8E-6	0.94 ± 0.01	7.7 ± 0.3
Cu@C <sub>3</sub> N <sub>4</sub>	16.8 ± 0.4	6.9E-06 ± 0.3E-6	0.90 ± 0.01	1.3 ± 0.1
G(CN)-Cu	16.2 ± 0.5	8.1E-06 ± 0.5E-6	0.95 ± 0.01	0.37 ± 0.01

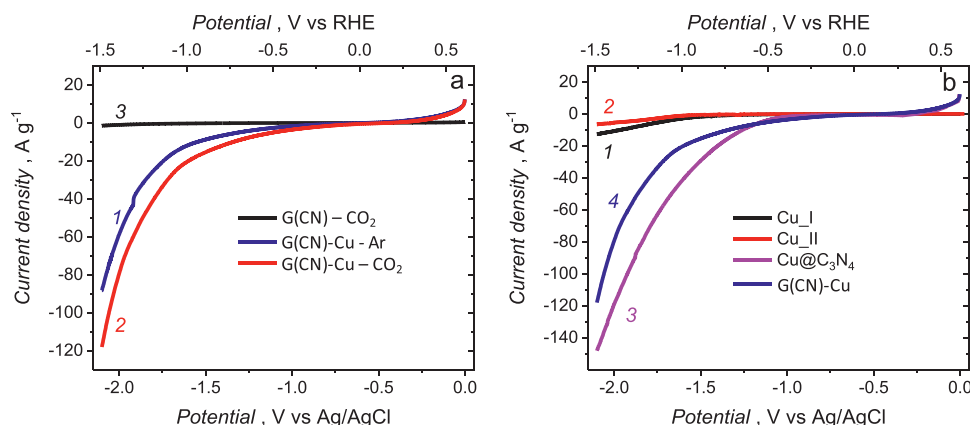


**Figure 5.** a) LSV curves for the G(CN)-Cu catalyst in the absence (curve 1) and presence of CO<sub>2</sub> (curve 2) as well as for the G-CN support in the presence of CO<sub>2</sub> (curve 3). b) Comparison of the Cu I, Cu II, Cu@C<sub>3</sub>N<sub>4</sub>, and G(CN)-Cu (curve 1, 2, 3, and 4, respectively) toward CO<sub>2</sub>RR. All LSV measurements were performed for 0.1 M KHCO<sub>3</sub> at 50 mV s<sup>-1</sup> scan rate.

mechanism.<sup>[16,2,49,50]</sup> Moreover, a Cu-based electrocatalyst presents less affinity to CO and can maintain excellent activity while the ratio between Cu(I) (easy to reduce/oxidize to Cu<sup>0</sup> and Cu(II)) is unchanged during the conducted reaction. For the performed electrochemical reaction, the G-CN provided excellent conductive communication between the redox couple Cu(II)-Cu(I) (cyclic intermediate) and mediated the charge transfer necessary for both MOR and CO<sub>2</sub>RR. The well-designed catalyst's

architecture enabled keeping the desired Cu(I)/Cu(II) species in balance, allowing for the partial reduction of Cu(II) to Cu(I) ions, leads to high MOR and CO<sub>2</sub>RR activity. The results obtained for CO<sub>2</sub>RR revealed that G(CN)-Cu catalyst outperforms the current state of the art material, presenting high current densities and lowering by 40–70% the reaction potential onset (Table 2). At the same time, the charge transfer resistance was also the lowest one among the reported materials for MOR.

**Table 2.** Catalysts performances in MOR and CO<sub>2</sub>RR.

Catalyst	Reaction	Peak current density		Reaction onset [V]	Charge transfer resistance [kΩ]	Ref.
		[mA cm <sup>-2</sup> ]	[mA mg <sup>-1</sup> ]			
Pt-C <sub>3</sub> N <sub>4</sub>	MOR	1.83 *	150	≈0.5	5–25	[54]
		6.42* (il.)	525 (il.)	≈0.5 (il.)	2–25 (il.)	
Pt/C <sub>N-doped</sub>	MOR	4.95–5.35	–	≈0.3	–	[55]
Pt/C	MOR	100	200*	≈0.4	≈0.5	[56]
NiO	MOR	20	–	≈0.45	1.5	[57]
Ni@/C <sub>3</sub> N <sub>4</sub>	MOR	12	57	≈0.35	0.12	[2]
		27 (il.)	127 (il.)	≈0.35	0.07	
Ni-Cu@C <sub>3</sub> N <sub>4</sub>	MOR	1.6	5.6	≈0.4	1.7	[2]
		2.7 (il.)	8.7 (il.)	≈0.4 (il.)	1.2	
Cu@C <sub>3</sub> N <sub>4</sub>	MOR	0.6	1.6	≈0.5	6.7	[2]
		0.9 (il.)	2.4 (il.)	≈0.5 (il.)	6.2	
G(CN)-Cu	MOR	14	63	≈0.4	0.4	Present work
Cu/C SAC	CO <sub>2</sub> RR	30	–	≈–0.6	–	[6]
Ni-SAC	CO <sub>2</sub> RR	24	–	≈–0.7	–	[58]
Cu-N5/HNPCS	CO <sub>2</sub> RR	11	–	≈–0.7	–	[58]
Au SAC	CO <sub>2</sub> RR	600	–	≈–0.6	–	[59]
Pt/C	CO <sub>2</sub> RR	27	–	≈–0.6	–	[60]
Cu@Pt/C	CO <sub>2</sub> RR	32	–	≈–0.6	–	[60]
Co-N5/HNPCS	CO <sub>2</sub> RR	35	–	≈–0.45	–	[47]
Cu@C <sub>3</sub> N <sub>4</sub>	CO <sub>2</sub> RR	36	150	≈–0.25	–	Present work
G(CN)-Cu	CO <sub>2</sub> RR	27	120	≈–0.25	–	Present work

(il.) – catalysts under visible light illumination. \*Calculated based on published data.

The main difference between G(CN)-Cu and Cu@C<sub>3</sub>N<sub>4</sub>, apart from the amount of Cu is the support type used to anchor the Cu active species, namely i) cyanographene (for G(CN)-Cu) and ii) carbon nitride g-C<sub>3</sub>N<sub>4</sub> nanosheets (for Cu@C<sub>3</sub>N<sub>4</sub>). G(CN)-Cu contains a smaller amount of Cu than Cu@C<sub>3</sub>N<sub>4</sub>; metal loadings in these systems expressed in wt% are 3.1 and 4, respectively. Moreover, the former catalyst is characterized by single atoms stabilized by -CN, while the latter by Cu nanoclusters, smaller than 1 nm, stabilized within the carbon nitride cavity, thus their growth and sintering are prevented during MOR.<sup>[1]</sup> The Cu@C<sub>3</sub>N<sub>4</sub> material, already characterized,<sup>[1,2]</sup> were used in this study as a reference sample. For this catalyst, the MOR reaction potential onset was found at 0.5 V with charge transfer resistance 6.7 kΩ. Although for G(CN)-Cu, the reaction potential onset was found to be similar to Cu@C<sub>3</sub>N<sub>4</sub> (0.4 versus 0.5 V), the charge transfer resistance was decreased by more than 90% (0.5 versus 6.7 kΩ). This can be related to the Cu sites' accessibility, stability, Cu-support interaction, and supports properties.

It is known that carbon nitride g-C<sub>3</sub>N<sub>4</sub> presents good conductivity in the parallel direction, that is, within the sheet, while the conductivity between stacking nanosheets is limited.<sup>[1,2]</sup> The electrical conductivity of the deposited films increases slowly with increasing nitrogen content up to ca. 12.8 at%.<sup>[53]</sup> Moreover, the graphitic carbon nitride films' measured electrical properties were related to the apparent film microstructure, bonding nature, and ambient humidity.<sup>[54]</sup> While comparing those films with carbon films deposited in pure Ar (which exhibits a dark resistivity at a room temperature of  $\approx 4 \times 10^{-2}$  Ωcm), the graphitic carbon nitride films deposited in pure N<sub>2</sub> were characterized by the resistivity of one order of magnitude lower. This effect was related to their denser morphology. The DFT study of 2D and 3D g-C<sub>3</sub>N<sub>4</sub> materials showed that 2D triazine and tri-s-triazine sheets are semiconductors as the graphene sheet (semiconductor type-n (triazine) and type-p (tri-s-triazine)), and besides are characterized by different porosity and adhesion energies. The 3D g-C<sub>3</sub>N<sub>4</sub> crystals were shown to have higher porosity than graphite, with 3D tri-s-triazine stacked sheets in configuration s<sub>2</sub> as the most porous, more than triazine or graphite (void spaces 84.7 and 86.9 versus 88.8). Thus they were proposed to have good properties allowing gas storage. Taking into account the band gaps, they are also extremely interesting for photochemical applications.<sup>[1,2]</sup> At the same time, the material presented lower adhesion energy (−0.67 s<sub>2</sub> and −0.49 s<sub>1</sub> J m<sup>−1</sup>) than both triazine and graphite (−0.28 and 0.31 J m<sup>−1</sup>). Thus the slow aging of those materials is expected.

On the other hand, the G(CN)-Cu is most likely more conductive than Cu@C<sub>3</sub>N<sub>4</sub>. This is due to different support – cyanographene, which was demonstrated as a highly conductive material.<sup>[51]</sup> Presumably, the lower Cu loading for G(CN)-Cu is compensated by atomic Cu dispersion and high site accessibility for electrochemical reactions, than in the case of Cu clusters on carbon nitride support. Although for Cu@C<sub>3</sub>N<sub>4</sub> the porosity was higher, the overall number of catalytically active sites for the electrochemical reaction was lower for this catalyst. Considering the pristine G-CN, its conductivity properties were related to the material preparation route. The applied preparation technique implied selective and effective nucleophilic substitution of fluoride ions in FG by −CN groups accompanied by reductive defluorination allowing for partial re-establishment of the delocalized π-electron cloud and good

conductivity as a consequence.<sup>[51,55]</sup> Moreover, the same study showed that electronic and magnetic properties of the functionalized graphenes are defined by the functionalization degree and nature of the functional group as well as the morphology arrangement of functionalities and sublattice symmetry, similar as in the case of g-C<sub>3</sub>N<sub>4</sub>. The functionalized graphenes were shown to exhibit high Young's modulus and strength, with the mechanical behavior strongly influenced by the van der Waals force.<sup>[56]</sup> According to literature, the fluorinated graphenes are considered to present ultrastrong adhesion.<sup>[56]</sup> However, they show similar adhesion energy to graphite. Thus the slow aging of those materials is expected, but still higher than the 3D carbon nitride support consisted of condensed tri-s-triazine stacked sheets characterized by adhesion energy −0.67 for s<sub>2</sub> type of stacking, also confirmed by XRD.<sup>[2]</sup>

Therefore, considering the physicochemical and structural properties of both Cu-based catalysts, a higher activity can be expected for G(CN)-Cu, due to higher Cu active site accessibility and better conductivity of the support, which provides better communication between Cu isolated atoms. This correlates very well with the obtained data for MOR (Figure 4). On the other site, reference Cu@C<sub>3</sub>N<sub>4</sub>,<sup>[2]</sup> presented comparable activity, owing to the higher Cu content, higher porosity (better gas diffusion properties), and good anti-aging properties for CO<sub>2</sub>RR. Moreover, the activities of both catalysts show a similar trend up to the potential  $\approx -1.23$  V versus Ag/AgCl (Figure 5). Below this value, the Cu@C<sub>3</sub>N<sub>4</sub> presents a slightly higher activity than G(CN)-Cu. This can be most likely related to fuel crossover and poison effects by different by-product formation and different activity of Cu@C<sub>3</sub>N<sub>4</sub> and G(CN)-Cu for electrochemical reaction and/or competitive electrochemical reaction of CO<sub>2</sub> and related by-products.<sup>[6]</sup> In the case of fuel crossover and poison effect, the chronoamperometric response of G(CN)-Cu indicates an excellent resistance to methanol poison, in correlation to literature.<sup>[6]</sup> The same study also showed superior electrochemical stability of single atom Cu-N-C catalysts (Cu single-atom catalyst with a high Cu content of over 20.9 wt% @ nitrogenated 2D carbon matrix). Besides, the authors showed no sensitivity to the carbon monoxide by atomic Cu. Therefore, according to DFT study, the high activity and material stability were correlated to favorable O<sub>2</sub> and OOH adsorption energies on Cu active sites, as well as improved molecular oxygen activation and O–O bond stretching on Cu-N<sub>2</sub> and Cu-N<sub>4</sub>.<sup>[35]</sup>

In the case of by-product formation a selectivity study was performed. In **Figure 6** the FE of the CO and H<sub>2</sub> CO<sub>2</sub>RR products distributions as the function of applied potentials from −0.4 to −1.2 V are displayed and compared with literature data.<sup>[6,35,57]</sup> For the G(CN)-Cu catalyst among the gaseous products H<sub>2</sub>, CO, and CH<sub>4</sub> were detected starting from −0.8 V versus RHE. It is worth noticing that hydrogen and CO production increased notably for lower potentials. The highest amounts of both gases were measured at −1.2 V. For methane, an inverse correlation to that observed for CO and H<sub>2</sub> was evidenced. This corresponds well with previously reported data.<sup>[6,35,57]</sup> In general, during CO<sub>2</sub>RR, apart from H<sub>2</sub>, CO, and CH<sub>4</sub> other products are reported, namely formic acid, ethanol, acetone, and ethylene, of which formation is voltage-dependent. The list of possible CO<sub>2</sub>RR products with the corresponding reactions and standard reduction potentials (E<sup>0</sup>) is given in **Table 3**.

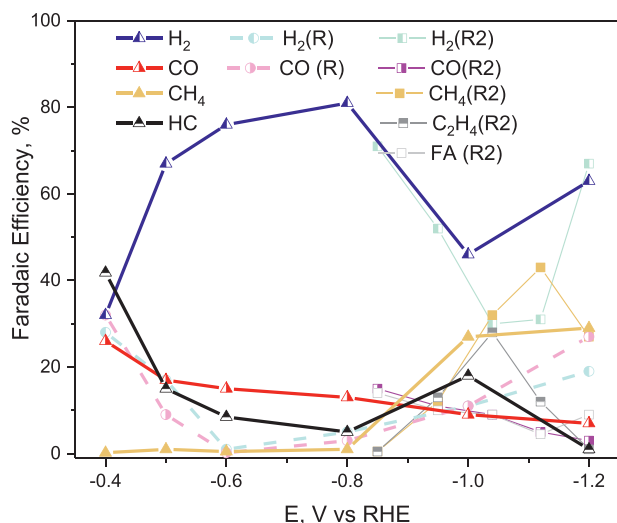


**Figure 6.** Faradaic efficiency for major products as a function of potential (HC—refers to other hydrocarbons than methane, R and R2 refer to the reference data plotted from literature<sup>[6,35,57]</sup>).

Usually, for Cu-based electrocatalysts, various HCs, including oxygenated HC, are detected, because Cu-sites facilitate the protonation of adsorbed CO intermediates.<sup>[6,35,57,58]</sup> The formation of selected HC is related to Cu-site structure and crystallographic facets exposed; ethylene, ethane, and C<sub>2</sub> HC were selectively formed on Cu(100) facets, while methane formation was mostly ascribed to Cu(111).<sup>[57,58]</sup> Moreover, it was shown that the size of Cu nanoparticles and pH also influenced the product distribution. While proton availability on the electrode decreases, C–C coupling prevails over protonation reaction. Thus for higher pH values, ethylene production is favored over methane. Further CO<sub>2</sub>RR conversion and product selectivity can be tuned by the size, structure, and oxidation state of the Cu-active sites (nanostructures, NPs).<sup>[6,35,57,58]</sup> Recently two competing catalytic pathways were postulated for CO<sub>2</sub>-to-ethanol reduction.<sup>[6]</sup> In the potential region of –0.4 V up to –0.8 V, ethanol was the main product of the CO<sub>2</sub>RR, while moving to a lower potential, the second pathway, resulting in enhanced CO and H<sub>2</sub> formation which were more pronounced. Moreover, it was shown that such a pathway is very sensitive to Cu loading and the state of Cu in the catalyst. Therefore, for different Cu loading on the electrocatalysts, various product distributions are usually reported.<sup>[6]</sup> It was shown that small Cu NPs promote CO and H<sub>2</sub> formation, while over bulk Cu CH<sub>4</sub> is detected as the

**Table 3.** CO<sub>2</sub>RR products with corresponding reaction mechanisms and standard reduction potentials (E<sup>0</sup>).<sup>[6,35,57]</sup>

Product	Reaction	E <sup>0</sup> versus RHE
CH <sub>4</sub>	CO <sub>2</sub> + 8e <sup>-</sup> + 8H <sup>+</sup> → CH <sub>4</sub> + 2H <sub>2</sub> O	0.17
C <sub>2</sub> H <sub>4</sub>	CO <sub>2</sub> + 12e <sup>-</sup> + 12H <sup>+</sup> → C <sub>2</sub> H <sub>4</sub> + 4H <sub>2</sub> O	0.06
CH <sub>3</sub> OH	CO <sub>2</sub> + 4e <sup>-</sup> + 4H <sup>+</sup> → CH <sub>3</sub> OH + 2H <sub>2</sub> O	0.02
H <sub>2</sub>	2H + 2e <sup>-</sup> → H <sub>2</sub>	0.0
HCOOH	CO <sub>2</sub> + 2e <sup>-</sup> + 2H <sup>+</sup> → HCOOH	-0.25
CO <sub>2</sub> <sup>-</sup>	CO <sub>2</sub> + e <sup>-</sup> → CO <sub>2</sub> <sup>-</sup>	-1.5

main product with a smaller amount of C<sub>2</sub> HC, H<sub>2</sub>, and traces of CO.<sup>[57,58]</sup> For our G(CN)-Cu catalyst a similar trend for the catalyst selectivity was observed as for single-atom Cu-catalysts reported previously, confirming the atomic Cu dispersion over G-CN and species stability during the performed reaction.

As was shown previously by density functional theory (DFT) calculations, the positive charge and spin density on copper was significantly decreased, and that charge transfer indeed facilitates the reduction of Cu(II) to Cu(I) for G(CN)-Cu.<sup>[12]</sup> Also, the tetragonal coordination environment for Cu single species has been confirmed as the most stable one, with the binding energy (BE) of –27.1 kcal mol<sup>-1</sup>.<sup>[12]</sup> The data for atomically dispersed Ni catalysts anchored on N-doped graphene (A-Ni-NG) showed that the monovalent Ni centers in the Ni–N<sub>4</sub> structure are the most active site, responsible for good CO<sub>2</sub>RR performance with a high CO selectivity at a moderate potential and desirable current density.<sup>[59]</sup> Similarly, the Ni–N<sub>4</sub> structure in the atomically dispersed Ni catalysts on N-doped carbon (Ni–N<sub>4</sub>-C), obtained through a topochemical transformation, was reported as the most active site for CO<sub>2</sub>RR.<sup>[60]</sup> For Ni–N<sub>4</sub>-C catalyst, an excellent selectivity toward CO over a wide potential range was demonstrated, with a Faradaic efficiency (FE<sub>CO</sub>) of 99% at –0.81 V (versus RHE). The higher selectivity of Ni–N<sub>4</sub>-C, compared with N-doped carbon (N-C), was attributed to the lower formation energy of COOH\* on Ni–N<sub>4</sub>.<sup>[60]</sup> It was also shown that apart from the Ni–N<sub>4</sub> structure, the Ni–N<sub>3</sub>C<sub>1</sub> can also be a possible active site of Ni-SACs, resulting in good CO selectivity. Among the 2D substrates-based SACs, Fe–N–C and Co–N–C and atomic Fe dispersed on N-doped graphene (Fe/NG) were reported.<sup>[14,32,49,50,60,61]</sup> For such electrocatalysts Fe–N<sub>4</sub> and Co–N<sub>4</sub> active sites were proposed to shape the overall catalysts' activities and selectivities toward CO, similarly as in the case Ni–N<sub>4</sub>-C.<sup>[49,62]</sup> A maximum FE<sub>CO</sub> of 93% was obtained for an Fe–N–C catalyst.<sup>[49]</sup> This value was higher than that obtained for Co–N–C (45%)<sup>43</sup> and Fe/NG (80% at 0.57 V).<sup>[62]</sup> The detailed active site structure and electronic state were investigated for Co–N–C,<sup>[50]</sup> which exhibited high selectivity for CO<sub>2</sub>RR with FE<sub>CO</sub> above 90% at a potential ranging from –0.57 to –0.88 V, and from –0.73 to –0.79 V exceeding 99%. The CO current density and FE<sub>CO</sub> were attributed to the catalytic activity of Co–N<sub>x</sub> species, of which activities decreased in the following order: Co–N<sub>5</sub> > Co–N<sub>4</sub> > Co–N<sub>3</sub>.<sup>[50]</sup> The experimental data and DFT calculations showed that single-atom Co–N<sub>5</sub> sites are most active centers, responsible for simultaneous CO<sub>2</sub> activation, the rapid formation of key intermediate COOH\* as well as the desorption of CO, providing high electrocatalytic stability (above 10 h).<sup>[50]</sup>

For our study, the HR-XPS N1s envelope (Figure S3, Supporting Information) as well as Cu 2p region, confirmed the charge transfer and the interaction between the N-atom from G-CN and Cu cations and the presence of paramagnetic Cu(II) centers in the catalyst together with Cu(I). At the same time, the formation of CuO nanoparticles/clusters has been not evidenced by performed HR-TEM and XRD study. Thus, the high activity of G(CN)-Cu (Figure 5) was related to the Cu single active sites with a low coordination number, which most likely is responsible for facilitating the activation of CO<sub>2</sub> to the CO<sub>2</sub><sup>-</sup> intermediate (rate-determining step (RDS) of CO<sub>2</sub>RR), similarly as was described for Co–N<sub>x</sub> catalyst. The presence of Cu(I) promotes binding and the activation of oxygen, initiating the



reaction, leading to a \*COOH intermediate, which guides the formation of CO or to higher-value added products (HCs/alcohols), as suggested for Cu-based catalyst.<sup>[63]</sup>

### 3. Conclusion

Graphene functionalized with nitrile groups (cyanographene) was ideal for immobilizing isolated copper atoms G(CN)-Cu. The rich electron lone pairs over G-CN were determined to provide abundant uniform nitrogen coordinators for Cu isolated atoms, with strong coordination, and the charged Cu(II) ions with partial reduction to Cu(I).

The G(CN)-Cu SACs revealed efficient electrochemical performance in MOR and CO<sub>2</sub>RR in alkaline solution. The excellent activity of G(CN)-Cu can be linked to the i) stable active site number with designed morphology: G(CN)-Cu present single active sites located at an unsaturated coordination environment; ii) single atoms location, their coordination, and interaction with support, which define the strength of adsorbate–surface interaction and hence influences on the surface electronic structure (Cu as the d-band center); iii) the neighboring Cu(I)/Cu(II) species/redox couple: cyanographene G-CN is conductive support, where the charge transfer is realized via –CN and the partially re-established delocalized  $\pi$ -electron cloud.

### 4. Experimental Section

*Preparation of Nanostructured Catalysts: Reagents and Materials.* Graphite fluoride (>61 wt% F, C1F1.1), NaCN (p.a.  $\geq 97\%$ ), N,N-dimethylformamide (DMF,  $\geq 99.8\%$ ), CuCl<sub>2</sub>·2H<sub>2</sub>O (99.99%). All solvents were HPLC grade. All aqueous solutions were prepared with ultrapure water (18 M $\Omega$  cm<sup>-1</sup>).

*Synthesis of G-CN and Metal Immobilization:* Cyanographene nanosheets were synthesized by following the authors' previous method.<sup>[12]</sup> Briefly, fluorinated graphite (120 mg,  $\approx 4$  mmol of C-F units) was added to 15 mL of DMF and stirred for 2 days. Then sonicated (Bandelin SONOREX, DT 255H type, frequency 35 kHz, power 640 W, effective power 160 W) for 4 h under nitrogen atmosphere. Then 800 mg of NaCN ( $\approx 16$  mmol) was added and the mixture was heated at 403 K with a condenser under stirring (500 rpm). After 2 days, the mixture was left to cool to room temperature. After washing and isolation of the pure product, the material was suspended in distilled water. Copper loading was achieved by mixing an aqueous suspension of G-CN (20 mL containing 120 mg of G-CN with CuCl<sub>2</sub>·2H<sub>2</sub>O (2 mL containing 60 mg of Cu ions). After 24 h of stirring, the mixture was separated with centrifugation. H<sub>2</sub>O was added in the pellet, mixed, and finally centrifuged in order to isolate the final copper-loaded G-CN. The catalyst (the copper-loaded G-CN) was finally freeze-dried and stored for further use. The determination of the copper content in the solid catalyst was performed with ICP-MS amounting to 3.1 wt%. The BET surface area of G(CN)-Cu catalyst was found to be 215 m<sup>2</sup> g<sup>-1</sup>.

*Characterization Techniques:* Powder XRD patterns of the material were determined by X'Pert Pro MPD diffractometer (PANalytical) in the Bragg–Brentano geometry, equipped with an X'Celerator detector and programmable divergence and diffracted beam anti-scatter slits at room temperature using iron-filtered Co-K $\alpha$  radiation (40 kV, 30 mA,  $\lambda = 0.1789$  nm). The angular range of measurement was set as  $2\theta = 5$ – $90^\circ$ , with a step size of 0.017°. Microscopic TEM images were obtained by HRTEM TITAN 60–300 with X-FEG type emission gun, operating at 80 kV. This microscope was equipped with Cs image corrector and a STEM high-angle annular dark-field detector (HAADF). The point resolution was 0.06 nm in TEM mode. The elemental mappings were

obtained by STEM-energy dispersive X-ray spectroscopy (EDS) with an acquisition time of 20 min. For HRTEM analysis, the powder samples were dispersed in ethanol and ultrasonicated for 5 min. One drop of this solution was placed on a copper grid with holey carbon film. XPS surface investigation has been performed on the PHI 5000 VersaProbe II XPS system (Physical Electronics) with a monochromatic Al-K $\alpha$  source (15 kV, 50 W) and photon energy of 1486.7 eV. Dual beam charge compensation was used for all measurements. All the spectra were measured in the vacuum of  $1.3 \times 10^{-7}$  Pa and at a room temperature of 21 °C. The analyzed area on each sample was a spot of 200  $\mu$ m in diameter. The survey spectra were measured with pass energy of 187.850 eV and an electron-volt step of 0.8 eV, while for the high-resolution spectra were used the pass energy of 23.500 eV and electronvolt step of 0.2 eV. The spectra were evaluated with the MultiPak (ULVAC–PHI, Inc.) software. All BE values were referenced to the carbon peak C 1s at 284.80 eV.

Multimode 8 microscope operating under PeakForce Quantitative Nanomechanical Mapping (PF QNM) mode was used for atomic force microscopy (AFM) imaging. PF-QNM mode operates in the PeakForce regime, where force-distance curves are collected for every pixel of the image. This mode allows for the simultaneous collection of information about sample topography and nanomechanical properties like Young's modulus, adhesion, etc. Highly ordered pyrolytic graphite (HOPG) was glued to the metallic disc using adhesive tape. Next, the HOPG was cleaved using a scotch tape to obtain an atomically flat substrate surface. The samples were prepared by drop-casting cyanographene (G-CN) or G(CN)-Cu suspension on the HOPG surface and then dried in air. The samples were imaged in air under room temperature using the ScanAsyst-Air probes from Bruker.

*Electrochemical Measurements:* Electrochemical measurements were performed using BioLogic Science Instruments and EC-Lab software from the same company. All the experiments were conducted at an ambient temperature and pressure. A three-electrode electrochemical cell with a 4-mm in diameter glassy carbon (GC), a graphite wire, and Ag/AgCl/KCl sat as working (WE), counter (CE), and reference (RE) electrode, respectively, were used.

Cyclic voltammetry (CV) and electrochemical impedance spectroscopy (EIS) were performed to study methanol (MeOH) electrochemical oxidation reaction (MOR) in the alkaline medium in the presence of 1.0 M NaOH.<sup>[2]</sup> CV measurements were conducted in the potential range of 0.00 to 0.80 V versus Ag/AgCl at a scan rate of 50 mV s<sup>-1</sup>. The EIS measurements were performed after an equilibrium state was established by applying a potential of 0.60 V versus Ag/AgCl for 60 s. After the current reached equilibrium, EIS was performed with voltage amplitude of 5 mV in a frequency range of 100 kHz to 10 mHz. EIS data analysis and modeling were performed by using ZView software (Scribner Associates Inc.).

Linear sweep voltammetry (LSV) in a 0.1 M KHCO<sub>3</sub> electrolyte solution was used to evaluate the electrocatalytic CO<sub>2</sub>'s electrochemical CO<sub>2</sub>RR. Before the measurement, the 0.1 M KHCO<sub>3</sub> aqueous electrolyte was saturated by CO<sub>2</sub> (99.999%) through purging for 1 h at pH 6.8, and a flow of CO<sub>2</sub> was maintained throughout the entire electrochemical measurement. The LSV measurements were performed in the potential range of 0.00 to  $-2.10$  V versus Ag/AgCl at a scan rate of 50 mV s<sup>-1</sup>.

The Cu I, Cu II, Cu@C<sub>3</sub>N<sub>4</sub> (4% Cu), and G(CN)-Cu(3.4% Cu) catalyst materials (5 mg) were dispersed in Milli-Q water (0.38 mL Millipore, ultrapure), in the presence of Nafion (57.8  $\mu$ L,  $\approx 5\%$  in a mixture of lower aliphatic alcohols and water, DuPont). The mixtures were sonicated for 30 min. Then, 15  $\mu$ L of the dispersed catalyst was deposited on the GC working electrode by drop-cast and allowed to dry for 24 h. All currents, measured during CV and LSV, were divided by the catalyst loading, taking into account the amount of Cu, and presented as the current density.

The electrochemical cell outlet was monitored with an online mass spectrometer HPR60 (Hiden). The FE<sub>CO</sub> (or H<sub>2</sub>) was calculated with the equation:

$$FE = n_{CO} \times F \times m_{CO} \times V_m / I \quad (1)$$

where  $n_{CO}$  is the number of electrons exchanged,  $F = 96485$  C mol<sup>-1</sup> (constant),  $m_{CO}$  is the mole fraction of CO in the gaseous mixture

analyzed,  $V_m$  is the molar flow rate in  $\text{mols}^{-1}$ , and  $I$  is the total current in A. The molar flow rate is derived from the volume flow rate  $V$  by the relation  $V_m = pV/RT$ ,  $p$  is the atmospheric pressure in Pa,  $R$  is  $8.314 \text{ J mol}^{-1} \text{ K}^{-1}$ , and  $T$  is the temperature in K.

## Supporting Information

Supporting Information is available from the Wiley Online Library or from the author.

## Acknowledgements

This research was supported by receiving funding from the NAWA The Polish National Agency for Academic Exchange through Bekker grants PPN/BEK/2019/1/00348 "C1-C4 alkanes to oxygenated fuel electrochemical transformation" and PPN/BEK/2019/1/00345 "Nanostructured carbon-based materials doped with metal nanoparticles as catalytic electrode materials for  $\text{CO}_2$  electroreduction with the use of surface-plasmon enhancement". M.A.M.K. extends his sincere appreciation to Researchers Supporting Project at King Saud University for funding this Research (RSP-2020/130). R.G.K., A.B., O.T., M.P., M.O., R.Z., and M.B.G. gratefully acknowledge the support by the Operational Program Research, Development and Education – European Regional Development Fund (project no. CZ.02.1.01/0.0/0.0/16\_019/000075 4) and by the ERDF project "Development of pre-applied research in nanotechnology and biotechnology" (project no. CZ.02.1.01/0.0/0.0/17\_048/0007323) of the Ministry of Education, Youth and Sports of the Czech Republic. R.Z. and A.B. acknowledge the support from the Czech Science Foundation, project No. 19–27454X. M.O. acknowledges support by the H2020 ERC project no. 683024. The research activity of D.M. was supported by funds from the European Union's Horizon 2020 research and innovation program under the Marie Skłodowska-Curie grant agreement No. 711859 and by financial resources for science in the years 2017–2021 awarded by the Polish Ministry of Science and Higher Education for the implementation of an international co-financed project.

## Conflict of Interest

The authors declare no conflict of interest.

## Author Contributions

I.S.P. and R.G.K. contributed equally to this work. I.S.P., P.P., D.M., R.N., R.K – AFM, electrochemical & modeling study; R.G.K., A.B., O.T., M.P., M.O., R.Z., M.B.G. – SACs synthesis and characterization.

## Keywords

Cu-catalyst, direct alcohol fuel cells, electrochemical methanol oxidation, N-doped carbon, single atom electrocatalysis

Received: October 16, 2020  
Revised: November 28, 2020  
Published online:

- [1] A. Lewalska-Graczyk, P. Pieta, G. Garbarino, G. Busca, M. Holdynski, G. Kalisz, A. Sroka-Bartnicka, R. Nowakowski, M. Naushad, M. B. Gawande, R. Zboril, I. S. Pieta, *ACS Sustainable Chem. Eng.* **2020**, *8*, 7244.

- [2] I. S. Pieta, A. Rathi, P. Pieta, R. Nowakowski, M. Holdynski, M. Pisarek, A. Kaminska, M. B. Gawande, R. Zboril, *Appl. Catal., B* **2019**, *244*, 272.
- [3] S. Zinoviev, F. Müller-Langer, P. Das, N. Bertero, P. Fornasiero, M. Kaltschmitt, G. Centi, S. Miertus, *ChemSusChem* **2010**, *3*, 1106.
- [4] S. Kumar, M. B. Gawande, J. Kopp, S. Kment, R. S. Varma, R. Zboril, *ChemSusChem* **2020**, *13*, 5231.
- [5] C. Xu, A. Vasileff, B. Jin, D. Wang, H. Xu, Y. Zheng, S. Z. Qiao, *Chem. Commun.* **2020**, *56*, 11275.
- [6] H. Xu, D. Rebolgar, H. He, L. Chong, Y. Liu, C. Liu, C.-J. Sun, T. Li, J. V. Muntean, R. E. Winans, D.-J. Liu, T. Xu, *Nat. Energy* **2020**, *5*, 623.
- [7] K. Faungnawakij, N. Shimoda, T. Fukunaga, R. Kikuchi, K. Eguchi, *Appl. Catal., B* **2008**, *341*, 139.
- [8] K. Faungnawakij, Y. Tanaka, N. Shimoda, T. Fukunaga, R. Kikuchi, K. Eguchi, *Appl. Catal., B* **2007**, *74*, 144.
- [9] R. González-Gil, C. Herrera, M. Á. Larrubia, P. Kowalik, I. S. Pieta, L. J. Alemany, *Int. J. Hydrogen Energy* **2016**, *41*, 19781.
- [10] P. Kowalik, K. Antoniuk-Jurak, M. Blesznowski, M. C. Herrera, M. A. Larrubia, L. J. Alemany, I. S. Pieta, *Catal. Today* **2015**, *254*, 129.
- [11] I. S. Pieta, M. Ishaq, R. P. K. Wells, J. A. Anderson, *Appl. Catal., A* **2010**, *390*, 127.
- [12] A. Bakandritsos, R. G. Kadam, P. Kumar, G. Zoppellaro, M. Medved, J. Tucek, T. Montini, O. Tomanec, P. Andryskova, B. Drahos, R. S. Varma, M. Otyepka, M. B. Gawande, P. Fornasiero, R. Zboril, *Adv. Mater.* **2019**, *31*, 190032.
- [13] A. T. Bell, *Science* **2003**, *5613*, 1688.
- [14] K. Kamiya, *Chem. Sci.* **2020**, *11*, 8339.
- [15] J. Resasco, A. T. Bell, *Trends Chem.* **2020**, *2*, 825.
- [16] J. Su, R. Ge, Y. Dong, F. Hao, L. Chen, *J. Mater. Chem. A* **2018**, *6*, 14025.
- [17] M. B. Gawande, A. Goswami, F. X. Felpin, T. Asefa, X. Huang, R. Silva, X. Zou, R. Zboril, R. S. Varma, *Chem. Rev.* **2016**, *116*, 3722.
- [18] W. Zang, Z. Kou, S. J. Pennycook, J. Wang, *Adv. Energy Mater.* **2020**, *10*, 1903181.
- [19] A. Liu, Y. Yang, X. Ren, Q. Zhao, M. Gao, W. Guan, F. Meng, L. Gao, Q. Yang, X. Liang, T. Ma, *ChemSusChem* **2020**, *13*, 3766.
- [20] I. S. Pieta, A. Donazzi, C. Resini, *Fuel Processing for Solid Oxide Fuel Cells*, **2018**, Springer, Cambridge pp. 97.
- [21] Y. Hou, Y. Liu, R. Gao, Q. Li, H. Guo, A. Goswami, R. Zboril, M. B. Gawande, X. Zou, *ACS Catal.* **2017**, *7*, 7038.
- [22] X. Li, J. Zhu, B. Wei, *Chem. Soc. Rev.* **2016**, *45*, 3145.
- [23] M. J. Lima, A. M. T. Silva, C. G. Silva, J. L. Faria, *J. Catal.* **2017**, *353*, 44.
- [24] G. Long, X. Li, K. Wan, Z. Liang, J. Piao, P. Tsiakaras, *Appl. Catal., B* **2017**, *203*, 541.
- [25] B. Singh, V. Sharma, R. P. Gaikwad, P. Fornasiero, R. Zbořil, M. B. Gawande, *Small* **2021**, <https://doi.org/10.1002/sml.202006473>.
- [26] B. Qiao, A. Wang, X. Yang, L. F. Allard, Z. Jiang, Y. Cui, J. Liu, J. Li, T. Zhang, *Nat. Chem.* **2011**, *3*, 634.
- [27] M. B. Gawande, P. Fornasiero, R. Zbořil, *ACS Catal.* **2020**, *10*, 2231.
- [28] G. Ha, Y. Zheng, X. Zhang, Z. Wang, Y. Gong, C. Du, M. N. Banis, Y.-M. Yiu, T.-K. Sham, L. Gu, Y. Sun, Y. Wang, J. Wang, Y. Gao, G. Yin, X. Sun, *Nano Energy* **2019**, *66*, 104088.
- [29] J. Xie, J. D. Kammert, N. Kaylor, J. W. Zheng, E. Choi, H. N. Pham, X. Sang, E. Stavitski, K. Attenkofer, R. R. Unocic, A. K. Datye, R. J. Davis, *ACS Catal.* **2018**, *8*, 3875.
- [30] Y. Zhu, W. Sun, W. Chen, T. Cao, Y. Xiong, J. Luo, J. Dong, L. Zheng, J. Zhang, X. Wang, C. Chen, Q. Peng, D. Wang, Y. Li, *Adv. Funct. Mater.* **2018**, *28*, 1802167.
- [31] M. Zhang, Y.-G. Wang, W. Chen, J. Dong, L. Zheng, J. Luo, J. Wan, S. Tian, W.-C. Cheong, D. Wang, Y. Li, *J. Am. Chem. Soc.* **2017**, *139*, 10976.
- [32] W. Liu, L. Zhang, W. Yan, X. Liu, X. Yang, S. Miao, W. Wang, A. Wang, T. Zhang, *Chem. Sci.* **2016**, *7*, 5758.

- [33] Y. Zhu, T. Cao, C. Cao, J. Luo, W. Chen, L. Zheng, J. Dong, J. Zhang, Y. Han, Z. Li, C. Chen, Q. Peng, D. Wang, Y. Li, *ACS Catal.* **2018**, *8*, 10004.
- [34] C. Gao, S. Chen, Y. Wang, J. Wang, X. Zheng, J. Zhu, L. Song, W. Zhang, Y. Xiong, *Adv. Mater.* **2018**, *30*, 1704624.
- [35] F. Li, G.-F. Han, H. J. Noh, S.-J. Kim, Y. Lu, H. Y. Jeong, Z. Fu, J.-B. Baek, *Energy Environ. Sci.* **2018**, *11*, 2263.
- [36] H. Yang, Q. Lin, C. Zhang, X. Yu, C. Zhong, G. Li, Q. Hu, X. Ren, Q. Zhang, J. Liu, C. He, *Nat. Commun.* **2020**, *11*, 593.
- [37] C. Wang, H. Zhao, J. Wang, Z. Zhao, M. Cheng, X. Duan, Q. Zhang, J. Wang, J. Wang, *J. Mater. Chem. A* **2019**, *7*, 1451.
- [38] G. Gao, Y. Jiao, E. R. Waclawik, A. Du, *J. Am. Chem. Soc.* **2016**, *138*, 6292.
- [39] B. C. Gates, M. Flytzani-Stephanopoulos, D. A. Dixon, A. Katz, *Catal. Sci. Technol.* **2017**, *7*, 4259.
- [40] X.-F. Yang, A. Wang, B. Qiao, J. Li, J. Liu, T. Zhang, *Acc. Chem. Res.* **2013**, *46*, 1740.
- [41] C. Zhu, S. Fu, Q. Shi, D. Du, Y. Lin, *Angew. Chem., Int. Ed.* **2017**, *56*, 13944.
- [42] J. Kim, H.-E. Kim, H. Lee, *ChemSusChem* **2018**, *11*, 104.
- [43] Q. Zhang, J. Guan, *Advanced Functional Materials* **2020**, *30*, 200076.
- [44] X. Zhang, J. Guo, P. Guan, C. Liu, H. Huang, F. Xue, X. Dong, S. J. Pennycook, M. F. Chisholm, *Nat. Commun.* **2013**, *4*, 192.
- [45] H. Fei, J. Dong, M. J. Arellano-Jiménez, G. Ye, N. Dong Kim, E. L. G. Samuel, Z. Peng, Z. Zhu, F. Qin, J. Bao, M. J. Yacaman, P. M. Ajayan, D. Chen, J. M. Tour, *Nat. Commun.* **2015**, *6*, 866.
- [46] K. Jiang, S. Siahrostami, A. J. Akey, Y. Li, Z. Lu, J. Lattimer, Y. Hu, C. Stokes, M. Gangishetty, G. Chen, Y. Zhou, W. Hill, W.-B. Cai, D. Bell, K. Chan, J. K. Nørskov, Y. Cui, H. Wang, *Chem* **2017**, *3*, 950.
- [47] H. B. Yang, J. Miao, S.-F. Hung, J. Chen, H. B. Tao, X. Wang, L. Zhang, R. Chen, J. Gao, H. M. Chen, L. Dai, B. Liu, *Sci. Adv.* **2016**, *2*, e150112.
- [48] B. Qiao, A. Wang, X. Yang, L. F. Allard, Z. Jiang, Y. Cui, J. Liu, J. Li, T. Zhang, *Nat. Chem.* **2011**, *3*, 634.
- [49] F. Pan, H. Zhang, K. Liu, D. Cullen, K. More, M. Wang, Z. Feng, G. Wang, G. Wu, Y. Li, *ACS Catal.* **2018**, *8*, 3116.
- [50] Y. Pan, R. Lin, Y. Chen, S. Liu, W. Zhu, X. Cao, W. Chen, K. Wu, W. C. Cheong, Y. Wang, L. Zheng, J. Luo, Y. Lin, Y. Liu, C. Liu, J. Li, Q. Lu, X. Chen, D. Wang, Q. Peng, C. Chen, Y. Li, *J. Am. Chem. Soc.* **2018**, *140*, 4218.
- [51] H. Yang, L. Shang, Q. Zhang, R. Shi, G. I. N. Waterhouse, L. Gu, T. Zhang, *Nat. Commun.* **2020**, *10*, 4585.
- [52] A. Bakandritsos, R. G. Kadam, P. Kumar, G. Zoppellaro, M. Medved, J. Tuček, T. Montini, O. Tomanec, P. Andryšková, B. Drahoš, R. S. Varma, M. Otyepka, M. B. Gawande, P. Fornasiero, R. Zbořil, *Adv. Mater.* **2019**, *31*, 190032.
- [53] W. Zhang, Y. Xia, J. Ju, L. Wang, Z. Fang, M. Zhang, *Solid State Commun.* **2003**, *126*, 163.
- [54] E. Broitman, N. Hellgren, J. Neidhardt, I. Brunell, L. Hultman, *J. Electron. Mater.* **2002**, *31*, L11.
- [55] D. D. Chronopoulos, A. Bakandritsos, M. Pykal, R. Zbořil, M. Otyepka, *Appl. Mater. Today* **2017**, *9*, 60.
- [56] S. Koenig, N. Boddeti, M. Dunn, J. S. Bunch, *Nat. Nanotechnol.* **2011**, *6*, 543.
- [57] J. W. Vickers, D. Alfonso, D. R. Kauffman, *Energy Technol.* **2017**, *5*, 775.
- [58] K. Zhao, X. Nie, X. Wang, S. Chen, X. Quan, H. Yu, W. Choi, G. Zhang, B. Kim, J. G. Chen, *Nat. Commun.* **2020**, *11*, 2455.
- [59] H. B. Yang, S. F. Hung, S. Liu, K. D. Yuan, S. Miao, L. P. Zhang, X. Huang, H. Y. Wang, W. Z. Cai, R. Chen, J. J. Gao, X. F. Yang, W. Chen, Y. Q. Huang, H. M. Chen, C. M. Li, T. Zhang, B. Liu, *Nat. Energy* **2018**, *3*, 140.
- [60] X. Li, W. Bi, M. Chen, Y. Sun, H. Ju, W. Yan, J. Zhu, X. Wu, W. Chu, C. Wu, Y. Xie, *J. Am. Chem. Soc.* **2017**, *139*, 14889.
- [61] H. Zhang, L. Li, S. Xi, Y. Du, X. Hai, J. Wang, X. Xu, G. Wu, J. Zhang, J. Lu, J. Wang, *Angew. Chem., Int. Ed.* **2019**, *58*, 14871.
- [62] C. Zhang, S. Yang, J. Wu, M. Liu, S. Yazdi, M. Ren, J. Sha, J. Zhong, K. Nie, A. S. Jalilov, Z. Li, H. Li, B. I. Yakobson, Q. Wu, E. Ringe, H. Xu, P. M. Ajayan, J. M. Tour, *Adv. Energy Mater.* **2018**, *5*, 1703487.
- [63] J.-H. Zhou, Y.-W. Zhan, *React. Chem. Eng.* **2018**, *3*, 591.